Gas desorption and electron emission from 1 MeV potassium ion bombardment of stainless steel

Arthur W. Molvik* and Michel Kireeff Covo
Lawrence Livermore National Laboratory, Heavy-Ion Fusion Virtual National Laboratory, Livermore, California 94550, USA

Frank M. Bieniosek, Lionel Prost,† Peter A. Seidl, David Baca, and Adam Coorey‡
Ernest Orlando Lawrence Berkeley National Laboratory, Heavy-Ion Fusion Virtual National Laboratory, 1 Cyclotron Road, Berkeley, California 94720, USA

Akira Sakumi
CERN, 1221 Geneva 23, Switzerland
(Received 5 April 2004; published 17 September 2004)

Gas desorption and electron emission coefficients were measured for 1 MeV potassium ions incident on stainless steel at grazing angles (between 80° and 88° from normal incidence) using a new gas-electron source diagnostic (GESD). Issues addressed in design and commissioning of the GESD include effects from backscattering of ions at the surface, space-charge limited emission current, and reproducibility of desorption measurements. We find that electron emission coefficients γ_e scale as $1/\cos(\theta)$ up to angles of 86°, where $\gamma_e = 90$. Nearer grazing incidence, γ_e is reduced below the $1/\cos(\theta)$ scaling by nuclear scattering of ions through large angles, reaching $\gamma_e = 135$ at 88°. Electrons were emitted with a measured temperature of ~30 eV. Gas desorption coefficients γ_0 were much larger, of order $\gamma_0 = 10^4$. They also varied with angle, but much more slowly than $1/\cos(\theta)$. From this we conclude that the desorption was not entirely from adsorbed layers of gas on the surface. Two mitigation techniques were investigated: rough surfaces reduced electron emission by a factor of 10 and gas desorption by a factor of 2; a mild bake to ~220° had no effect on electron emission, but decreased gas desorption by 15% near grazing incidence. We propose that gas desorption is due to electronic sputtering.

DOI: 10.1103/PhysRevSTAB.7.093202 PACS numbers: 41.75.Ak, 52.58.Hm, 79.20.Rf, 34.50.Dy

I. INTRODUCTION AND SUMMARY

Beam-induced pressure rises [1] and electron cloud effects [2] are frequently observed to limit the performance of colliders and other high-intensity rings. These may also limit the performance of future high-intensity heavy-ion accelerators such as envisioned as drivers for heavy-ion inertial fusion (HIF) [3]. The cost of accelerators for HIF can be reduced by fitting beam tubes tightly to beams. This places them at risk from a steady pressure rise, production of secondary electrons, and consequent loss of beam control. We have therefore initiated a coordinated program to measure electron emission and gas desorption by 1 MeV K^+ ions incident on a stainless steel target near grazing incidence, to measure gas and electrons in drift regions and magnetic quadrupoles of HIF accelerators [4], and to model these effects [5,6]. The 1 MeV energy range is typical of injectors and, as will be discussed, is appropriate to ongoing studies of the hypothesis that gas desorption from ion impact on metal walls is through the mechanism of electronic sputtering. This paper describes our procedure and results in the first area of study: measuring electron emission and gas desorption.

Electron emission due to ion impact on surfaces has been studied extensively. Papers that cover a wide range of ion species, energies, and angles are listed below; each contains additional references. Electron emission coefficients γ_e, from ion impact on 304 stainless steel at angles ranging from normal to near grazing incidence, have been studied by Thieberger *et al.* for 28 MeV protons, 126 MeV oxygen ions, and 182 MeV gold ions. They found $\gamma_e \propto 1/\cos(\theta)$ to near grazing incidence, reaching values of $\gamma_e = 148$, 6460, and 28 000, respectively [7]. Clouvas *et al.* measured emission from ion impact at normal incidence on a thin carbon foil, using 15 different ions from mass 1 to 73 at energies from 1 to 34 MeV. They measured emission from both sides of the foil separately, and showed that the yield scaled with the electronic stopping power with values ranging from $\gamma_e = 0.3$ to $\gamma_e = 194$ [8]. Itoh *et al.* found similar results with atomic and molecular ions with mass from 1 to 32, and between 0.3 and 2.0 MeV incident on gold [9]. Electron emission from very low energy ions is reported to yield $\gamma_e \leq 1$ by Kanie *et al.* [10]. Other work has been done in a different regime, where the potential energy of a highly charged

*Electronic address: molvik1@llnl.gov
†Current address: Fermi National Accelerator Laboratory Batavia, Illinois 60510, USA.
‡Permanent address: Department of Mathematics and Computer Science, University of California, Los Angeles, CA, USA.

ion greatly exceeds its kinetic energy [11,12]. We measure γ_e with 1 MeV K^+ ions to follow a $1/\cos(\theta)$ scaling from 80° to 86° where $\gamma_e = 90$. Nearer grazing incidence, γ_e is reduced below the $1/\cos(\theta)$ scaling by nuclear scattering of ions through large angles, reaching $\gamma_e = 135$ at 88°.

Gas desorption coefficients have been published for both much higher and much lower energy heavy ions at various angles of incidence. Mahner *et al.* [13] measured gas desorption coefficients ranging from as high as 25 000, to below 100 after beam scrubbing, due to 800 MeV lead ions impacting clean (chemically cleaned, vacuum fired, and finally baked *in situ*) stainless steel. Desorption rates of $\sim 10^4$ have been inferred from the decay time of 10–150 MeV/u U^{28+} ions in the GSI synchrotron SIS [14]. Much higher desorption rates have been obtained from a 1.5 μm thick amorphous C:H layer on a substrate: 7×10^6 hydrogen atoms and 2.3×10^6 carbon atoms desorbed per incident 100 MeV iodine [15] measured with elastic recoil detection analysis. For very low ion energies, e.g., 500 eV noble gas ions [16] and 300–1500 eV hydrogen ions [17], desorption coefficients below one were consistent with knock-on collisions (nuclear large-angle scattering). We measure desorption coefficients in the range of 3800–15 000 depending upon surface conditions and the assumptions used in analysis of changes in pressure.

The High-Current Experiment (HCX) at LBNL is used to study the transport dynamics of a 1 MeV, 180 mA, K^+ ion beam [18,19]. (The injector has also operated at 1.8 MeV, 600 mA.) The base pressure ranges from mid 10^{-8} torr to low 10^{-7} torr range. The 1 MeV beam has a space-charge potential of $\sim$2 kV, a current rise time of 250 ns (10%–90%) and fall time of 1 μs, a flattop duration of 4 μs, and a pulse repetition time of $\sim$10 s. We measure the flux of electrons and gas evolved from a target, whose angle to the beam can be varied between 80° and 88° from normal incidence in the GESD on the HCX. These angles overlap the angles of incidence of halo ions that are lost to the walls. For a 1.8 MeV beam in HCX, loss angles would be in the range of 87° to 90° after transport through 10 m (50 quadrupoles) [6].

The GESD results are needed to interpret the current from electrodes that are flush with the beam tubes in quadrupole magnets [4]. Using the electron emission coefficient measured with the GESD, we can infer the beam-halo loss that caused the electron emission. Then using the measured gas desorption coefficient, we can infer the resulting gas desorption. The GESD results also provide constraints for design of future experiments and accelerators and the GESD can be used to study mitigation techniques for reducing electron emission and gas desorption. In addition, these results bear on the problems of electron emission from ion impact, for which empirical models are successful [6,7], and on gas desorption or sputtering from ion impact on a metal surface, a poorly understood area of basic atomic/surface physics [1]. One indication of how little this area is studied and understood, is that it does not have a PACS number, unlike photon and electron stimulated desorption (79.20.La).

This paper is organized as follows: In Sec. II we discuss the design of the GESD that, in addition to the usual issues such as secondary electron suppression, includes evaluation of beam ions scattered off the target surface and reproducibility of gas desorption measurements. In Sec. III, we discuss the commissioning of the GESD including validating measurements of the electron emission current from the target and the ion beam current into the GESD, as well as the calibration of the ion gauge in its modified surroundings. In Sec. IV we observe the usual $1/\cos(\theta)$ dependence of electron emission on K^+ angle of incidence (θ) and explain departures from it near grazing incidence, discuss errors that would arise from space-charge limited current of secondary electrons, demonstrate the validity of our measurements, and make an approximate measurement of the energy distribution of emitted electrons. Finally, in Sec. V we discuss measurements of ion-induced gas desorption, its dependence on angle of incidence, two mitigation techniques, surface impurity characterization, and a proposed model for desorption.

II. DESIGN OF THE GESD

The GESD is shown in Fig. 1. It consists of several electrodes, to measure the electron emission coefficient at angles of incidence varying over 80°–88° from normal, and an ion gauge to measure the total gas desorption coefficient. After an entrance aperture, the electrodes include an electron suppressor, the solid front support for the grid, the target, and the scattered-ion catcher in

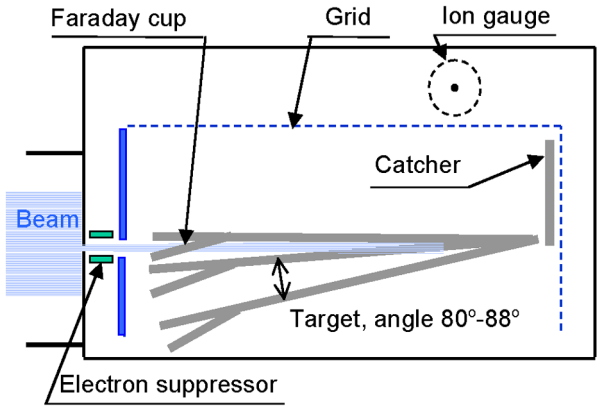

FIG. 1. (Color) The gas-electron source diagnostic (GESD) measures electron emission and gas desorption caused by an ion beam, incident from the left on a target at grazing angles. The target is shown at three possible angles, the upper position exposes a Faraday cup under the target to the ion beam.

that order, plus a Faraday cup under the target. Each electrode can be biased independently.

An entrance aperture, 0.3 cm high by 2.5 cm wide, transmits a small area from near the center of the beam which has expanded to a radius as large as 25 cm over a 1.7 m drift distance from the last transport quadrupole. The apertures in subsequent suppressor (and grid supports) are larger: 0.5 cm (0.6 cm) in height and 2.8 cm (3.3 cm) in width to prevent ion impingement. The suppressor extends 1 cm along the beam.

The normalized beam emittance is 0.5π mm mrad in an $r_b = 11$ mm radius beam. For a beam velocity $\beta = v/c = 0.007$, after expansion to a 250 mm radius, the expansion angle x' will be

$$x' = \frac{\epsilon_n}{\beta r_b} = 0.29 \text{ mrad}. \quad (1)$$

This half-angle expands the beam by only 0.05 mm in the 18.5 cm from the entrance aperture to the hinged end of the target. The back (right) of the target extends above a projection of the top of the aperture by this distance plus an alignment tolerance of 1 mm to ensure that all primary beam ions admitted through the aperture strike the target.

Beam ions strike near the back of the 15 cm long by 9 cm wide target. It is made of 0.18 cm thick stainless steel which is hinged at the right, so that the angle of incidence can be varied. It can be biased to measure electron emission current. Its surface has been sanded to remove short wavelength departures from flatness. This used a medium grit aluminum-oxide paper, finishing with Scotch-Brite (a mild abrasive pad). Compared with machined comparison plates, the target roughness appears to be ~ 32 μin. (~ 1 μm). The sanding grooves were aligned parallel to the beam direction to minimize the "ploughed-field" variations in ion angle of incidence on a microscopic scale.

Electrons are prevented from entering or leaving the GESD by the electron-suppressor electrode. The grid can be operated either to suppress or to encourage electron emission from the target. Near the entrance aperture, the end support is solid metal 0.3 cm thick, which augments the operation of the electron suppressor when it is negative. The mesh portion of the grid resembles a covered wagon wrapped around the top and sides of the target with a length of 17 cm. It is made of woven 304 stainless steel with 20 mesh/cm, a transparency of 90%, and is spaced 5 cm from the target near the hinge.

A. Ion backscattering from surfaces

During the design, we identified a problem that complicated using the target to measure the ion beam current into the GESD. The SRIM Monte Carlo code computes the slowing and scattering of ions in matter [20]. It predicts that, near grazing incidence, 0.6–0.7 of 1 MeV K^+ ions would backscatter as shown in Fig. 2. (We are using the term "backscatter" to mean not a scattering by an angle greater than 90°, but a scattering back out of a surface. This corresponds to the usage in the SRIM code. For ions near grazing incidence, backscatter in our usage can refer to scattering by an angle $\ll 90°$.) The physics in the SRIM code has been discussed in detail [21]. From a series of SRIM runs at different angles and evaluating the beam scattering from the bottom, middle, and top of the 0.3 cm high beam, we determined that a 4.5 cm high ion catcher shown would capture $f \geq 90\%$ of the scattered ions.

We estimate the secondary electron current from the grid to the target (I_{T-se}), when the grid is biased to suppress secondary emission from the target, Eq. (2).

$$I_{T-se} = \gamma_e(1-T)(1-f) \leq 0.2, \quad (2)$$

where we used typical electron emission coefficients of $\gamma_e \leq 20$, previously observed for MeV range K^+ ions near normal incidence [22], and a grid transparency of $T = 90\%$. This indicates that the uncertainty from using the target to measure the beam current will be as much as 20% due to electron emission from the grid. This provides motivation to use a Faraday cup to obtain a more accurate measurement of the beam current into the GESD, as will be discussed in Sec. III B.

We repeated the SRIM computational runs at different angles, Fig. 3, but using slightly higher energy ions, 1.8 MeV rather than the 1.0 MeV ions used in the experiments presented here, and in the calculations shown in Fig. 2. We see that the fraction of ions backscattered drops rapidly at angles further from grazing incidence (90°): from 0.6–0.7 at 88° to 0.0005 at 0°.

We also studied ion backscatter as a function of ion energy, from 1 to 1000 MeV K^+ at angles of 89°, 85°, and 0°, Fig. 4. Near grazing incidence, ion backscatter (reflection) remains high out to energies exceeding

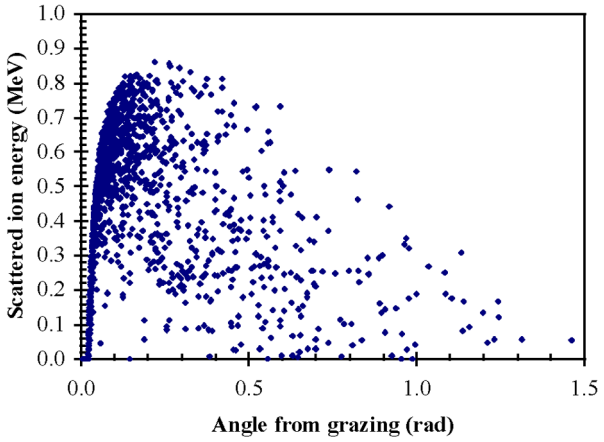

FIG. 2. (Color) Energy versus angle of the 1355 back scattered ions from 2000 1 MeV K^+ ions incident on stainless steel at 88° from normal, computed by the SRIM code. Except for this figure, angles are shown relative to normal incidence.

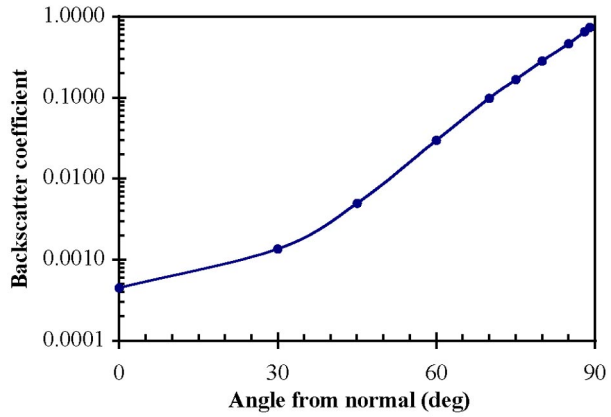

FIG. 3. (Color) Fraction of 1.8 MeV K^+ ions that backscatter off of stainless steel versus angle of incidence, computed by the SRIM code. For angles $\geq 45°$, the backscatter e-folds in 8.5°.

100 MeV. Near normal incidence, the ion backscatter starts low and decreases rapidly with energy. We see that for minimum ion reflection from a wall the ideal is either a sawtooth surface on the wall (tested on the SPS for application to the LHC at CERN [23]) or a series of apertures to scrape the beam halo, where the apertures are closely spaced so that beam cannot strike the wall between them.

B. Gas desorption

Our goal here is to characterize desorption from target surfaces similar to those used in our present accelerators, so we had the target treated with the LBNL ultrahigh vacuum (UHV) cleaning procedures [24]. In this procedure parts are cleaned with hydrocarbon solvents then with detergents until sheeting occurs, rinsed first with tap water and then deionized water, and blow-dried with oil-free nitrogen. The beam-facing surfaces are not baked, either before final assembly or *in situ*, except as otherwise described. The desorption coefficients that we measure are therefore likely to be higher than those for baked surfaces in Ref. [13] if we had a validated physics model that would allow comparison of desorption due to different beam species and energies incident on specified surfaces.

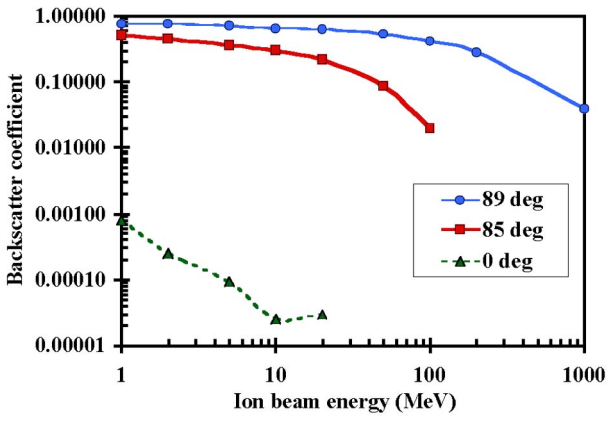

FIG. 4. (Color) Fraction of K^+ ions that scatter off of stainless steel versus ion energy at three selected angles, computed by the SRIM code.

The total gas desorption coefficient γ_0 is measured from the pressure rise after a pulse. The GESD is enclosed in a stainless steel box with internal dimensions of 12.7 cm width, 15.2 cm height, and 23.2 cm length. Joints use metal-to-metal machined surfaces which are not vacuum tight. It is installed in a cylindrical vacuum tank 33 cm inside diameter and 74 cm long that bolts onto the end of the HCX. The GESD pumps out through the 0.3×2.5 cm rectangular entrance aperture, and a 1 cm diameter hole on the back wall behind the catcher. This, together with the internal volume $V = 4180$ cm^3 of the GESD (after subtracting 306 cm^3 for the internal structures), gives a measured pump-out time constant of $\sim$0.3 s, long enough for an ion gauge to determine the peak pressure, but short compared with the $\sim$10 s before the next pulse.

An implicit assumption in deriving a desorption coefficient from the pressure rise is that the desorbed molecules can undergo many collisions with the wall, while the pressure is being measured, without sticking to the wall or knocking more molecules off the walls. Chapter 2.4 of Ref. [25] discusses the physics basis for these issues. Although the data are insufficient to prove the validity of these assumptions, two points are worth noting: (i) Sticking coefficients range between 0.1 and 1.0 for clean tungsten with a fractional monolayer coverage of gas, but decrease to less than 0.001 as the coverage approaches one monolayer (see Figs. 2.22 and 2.27 of Ref. [25]). (One monolayer is between 5 and 10×10^{14} molecules/cm^2, depending on the size of the molecules; see Table 2.28 of Ref. [25].) (ii) From the same table, the sojourn time that a molecule remains on a surface before being desorbed again can range up to seconds for ≤ 0.01 monolayer, but decreases to 320 μs at 1.0×10^{14} molecules/cm^2. The sojourn time can be measured from the transmission delay of a pressure pulse through a capillary tube. When the gas layer is thick enough that the sojourn time no longer varies with gas coverage, the sojourn time has decreased further to less than 10^{-12}, 10^{-10}, and 10^{-4} s for H_2, N_2, and an organic molecule, respectively (see Table 2.30 and associated discussion in [25]).

We measure the pressure rise with a Bayard-Alpert ion gauge. As shown in Fig. 1, the ion gauge views the target; this was intended to allow time-of-flight measurements of desorbed gas velocity. Possible problems with this position include scattered beam ions and secondary electrons striking electrodes of the ion gauge and desorbing

gas from them. This could cause an immediate pressure rise in the vicinity of the gauge; however, we waited a minimum of 50 ms after the 5 μs beam pulse before beginning to analyze the pressure change. This provides a minimum of 100 collisions with the wall for gas within the GESD, so the pressure should be equilibrated. The gauge should respond on the ~100 μs time scale for gas to cross the 1.5 cm diameter grid. The preamplifier used also has a rise time of 100 μs. As is required to measure the peak pressure rise, these times are small compared with the GESD pump-out time of 0.3 s.

The ion gauge is powered by dc power supplies that provide bias voltages of +180 V to the grid, and +22 V to the filament and its floating heater power supply. These eliminate changes in the filament heater current produced by feedback regulation during a transient pressure rise. A meter in series with the filament bias supply is read at the time of each shot to obtain the filament emission current. The emission current is adjusted with the heater supply. A current-to-voltage preamplifier is used on the collector signal to drive ~30 m of coaxial cable to the digital recorders. It is separated from the collector by a minimum length of coaxial cable, approximately 0.6 m inside and 0.3 m outside the vacuum. Ion gauges, or residual gas analyzers, measure only volatile molecules that can impinge walls many times without sticking; metal atoms that sputter will not be measured here because they are likely to stick to the first surface that they impinge.

A capability of a mild *in situ* bake (to ~220 °C) is provided by a heating element within the GESD box. Thermocouples are mounted on the bottom of the target and on the box to monitor temperatures.

III. COMMISSIONING OF THE GESD

Commissioning is discussed in three subsections: III A measuring current-voltage characteristics for each electrode, and selecting operating points where reliable electron emission coefficients can be determined, III B validating a measurement of the beam current into the GESD, and III C calibrating the ion gauge used to measure the gas desorption.

A. Electron-emission current

Initial tests showed that the suppressor bias voltage should be at least as negative as −30 V to prevent electrons entering or leaving the GESD with the beam. We operated it at −200 V for most of the data shown in this paper (except for the data in Fig. 12 where the suppressor bias was −50 V). The catcher bias was varied to minimize its current, a bias of −25 V with the target biased at −40 V appeared optimum to keep the catcher current small compared with the target current. We observed that the sum of the target plus catcher current is nearly constant at − 0.234 ± 0.026 mA. The target bias voltage was chosen to be −40 V based on observations that the target current became increasingly negative for positive target bias (with the grid at −150 V to suppress electron emission from the target) and that the target current was nearly constant for a target bias of −20 to −60 V. A catcher bias of −25 V, with the target at −40 V, has become our standard operating point.

With these established, we measured the target current as a function of varying grid bias, Fig. 5(a). The target current is observed to saturate for positive grid biases exceeding 50 V. Operation in this regime assures us that we are measuring a current that is emission limited; that is, we measure every electron emitted as is required to obtain electron emission coefficients. If the target current were space-charge limited, some emitted electrons would return to the target and we would observe the current continuing to increase with higher grid bias voltage. We find that a grid bias more positive than the target by 90 V is sufficient to obtain reliable target electron emission current.

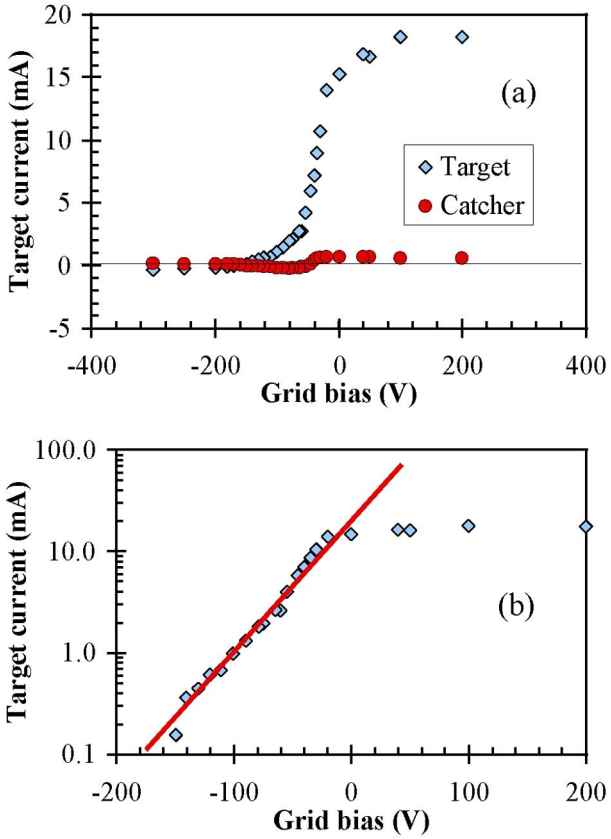

FIG. 5. (Color) The bias voltage of the grid is varied, one shot at each bias, while maintaining the target at −40 V and an angle of 80° from normal incidence, the suppressor at −200 V and the catcher at −45 V. A grid bias more positive than the target by 90 V is sufficient to obtain reliable target electron emission current. (a) The target current (blue diamonds) and catcher current (red circles) displayed on a linear scale and (b) the target current is displayed on a log scale for ease in comparing with a 30 eV exponential fit (red line).

B. Beam current into GESD

The beam current into the GESD is measured with a U-shaped Faraday cup to obtain the electron emission coefficient. It is installed under, and insulated from, the target. The Faraday cup was tested to ensure that the current was independent of the electrode bias potentials, that the measured beam currents were constant for small shifts of position off center, and that they changed symmetrically either side of center for larger shifts, Fig. 6. The current increases farther off center where the beam hits the outside of the Faraday cup, generating secondary electrons that are not suppressed but flow to the target or to the grounded box.

The HCX beam is expanding over the 1.7 m drift to the GESD, so that the current into the GESD is measured to be ~0.14 mA, out of a total beam current of 180 mA at 1 MeV. Maintaining the ion beam current at $\ll 1$ mA is necessary to avoid limiting the electron emission current by space charge [26] rather than by electron emission. This is also expected to desorb ≤ 0.1 monolayer of gas per pulse, which we obtained as follows: We used our earlier data for 80 keV K^+ incident on stainless steel targets at angles ranging between 0° and 80° from normal for which we measured desorption coefficients ranging between 1000 and 1500, depending on the angle of incidence [27]. In lieu of an accepted model for gas desorption, we used the hypothesis that we could scale desorption with a plausible upper limit of E_b^1 and lower limit of E_b^0, where E_b is the beam energy. For the HCX beam parameters, this extrapolates to an upper-limit beam-desorption coefficient approaching 20 000. (We will show evidence that the observed gas desorption is not primarily from adsorbed layers of gas on the surface; nevertheless, we believe that this criterion provides a reasonable basis for expecting reproducible desorption measurements over a scan of up to 50 shots.)

We control the beam current into the GESD to meet these criteria, so that a current-voltage characteristic for the target or grid voltage shows the electron emission current nearly constant for a range of bias voltages, Fig. 5(a), rather than increasing with bias voltage as it would for space-charge limited current. We have reduced the beam current by varying the focusing strength of the final electrostatic quadrupole, QI10. In Fig. 7 we plot the Faraday cup current as function of QI10 bias, and we also show the calculated current into the GESD 0.3×2.5 cm entrance aperture from the beam expansion to twice-rms elliptical radii a and b at the GESD as predicted from an envelope code and the total beam current $I_{b-\mathrm{HCX}}$ measured with a large Faraday cup, Eq. (3). The similarity of these independent determinations of the beam current into the GESD is further evidence that the Faraday cup measurement of beam current into the GESD is reliable. Based on these results, we operate QI10 at 40 kV with the GESD, compared with 24.43 kV for matched beam transport:

$$I_{\mathrm{envel}} = \frac{(0.3\ \mathrm{cm})(2.5\ \mathrm{cm})}{\pi ab} I_{b-\mathrm{HCX}}. \qquad (3)$$

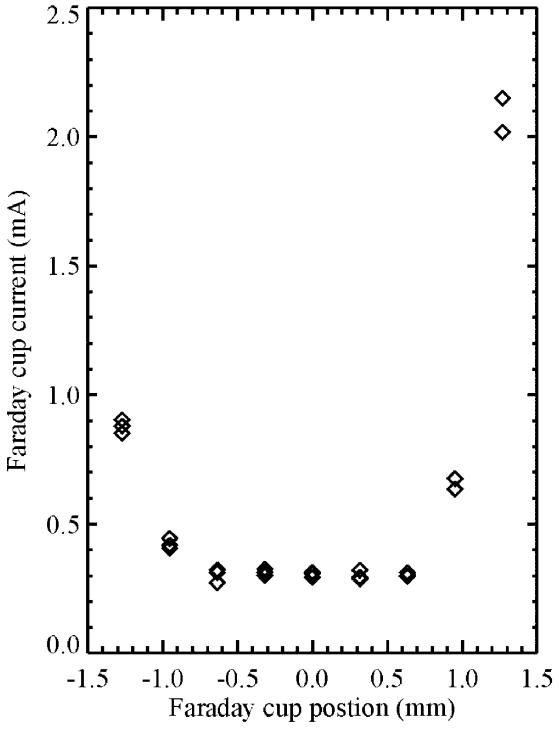

FIG. 6. The beam current measured by the Faraday cup as a function of its position, relative to centered on the entrance aperture.

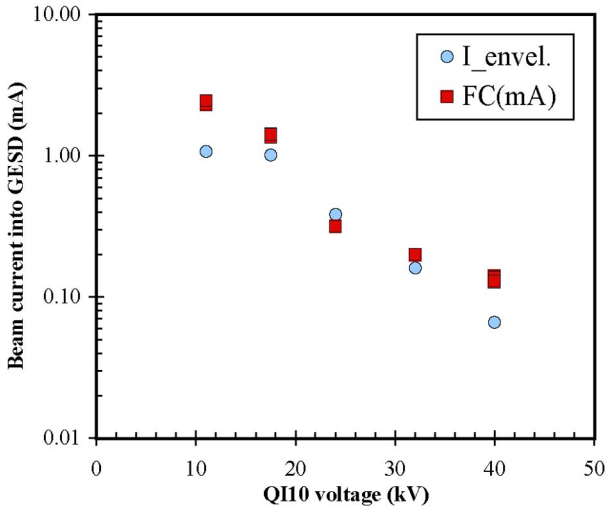

FIG. 7. (Color) Beam current into the GESD measured with the Faraday cup inside the GESD (red squares) and inferred from the total beam current times the entrance aperture area divided by the area that the beam is predicted to expand to at the GESD (blue circles) as the voltage on the final electrostatic quadrupole QI10 is varied.

The beam is not perfectly uniform, so the agreement in Fig. 7 is reasonable between a small area measured near the center of the beam with the Faraday cup inside the GESD and that inferred with Eq. (3) [19].

C. Pressure calibration

The ion gauge is surrounded by a grounded stainless steel woven mesh of about 0.5 transparency to prevent the filament emission current from varying with the bias on the nearby GESD grid. When thus shielded, the gauge emission current varied by $\leq 2\%$ when the GESD grid bias varied by ± 100 V. We calibrated the ion gauge, with the cylindrical mesh installed, against a Granville Phillips Stabil-Ion gauge. The calibration extended over a range of emission currents from 0.5–10 mA and at two pressures of 0.7 and 2.5×10^{-6} torr, Fig. 8. The pressure P and calibration constant K are related by

$$P(\text{torr}) = \frac{I_{\text{coll}}}{I_{\text{emis}} K}. \tag{4}$$

The sensitivity varied by 13% with emission current, from a low of 7.7 torr^{-1} at 2 mA to about 8.7 torr^{-1} approaching 10 mA. This compares with the nominal calibration constant of 25 torr^{-1} for Bayard-Alpert nude ion gauges. The base pressure inside the GESD is usually in the 10^{-6} torr range, an order of magnitude or more higher than the base pressure of the accelerator it is installed in because of the intentionally slow pump-out time of ~ 0.3 s.

IV. ELECTRON EMISSION

A. Dependence on ion angle of incidence

The electron emission coefficient γ_e is determined by the ratio of the electron emission current leaving the target I_e to the beam current into the GESD I_b. In practice, since the total target current I_t is given by $I_t = I_e + I_b \approx I_e$, we use the simple ratio of I_t/I_b in determining γ_e. To measure the electron emission current, we bias the grid to $+150$ V and the scattered-ion catcher to -25 V, with the target at -40 V. The beam current of 1 MeV K^+ into the GESD is measured with a Faraday cup as described in the previous section. The electron emission coefficient is shown versus θ, the ion angle of incidence relative to normal, in Fig. 9. (Here we show data for which the target was baked a total of 85 h at $\sim 220\,^\circ$C because it is a larger data set than the prebake data, with which it will be compared later.) The $1/\cos(\theta)$ curve shown is a good fit to data at angles from 80° to 86°. At larger angles, closer to grazing incidence, the data fall below the $1/\cos(\theta)$ curve. The close fit below 86° to $1/\cos(\theta)$ is surprising with our unpolished target surface; we would expect sanding to leave roughness on a microscopic scale of grain sizes, of order ~ 10 μm. The range of 1 MeV K^+ ions in stainless steel is only 0.5 μm, which is too small to average over such roughness.

These results are consistent with a model based on electron energy input from ion beam, dE/dx, in matter. This model can be described briefly: as an ion enters a surface, it loses energy by interacting with electrons in the material. Electrons that are pulled free from their bonds to atoms are called delta electrons. Some delta electrons that originate sufficiently close to the surface can escape the surface, resulting in electron emission. Delta electrons formed below a certain depth cannot escape the surface [7,28]. This model predicts the depen-

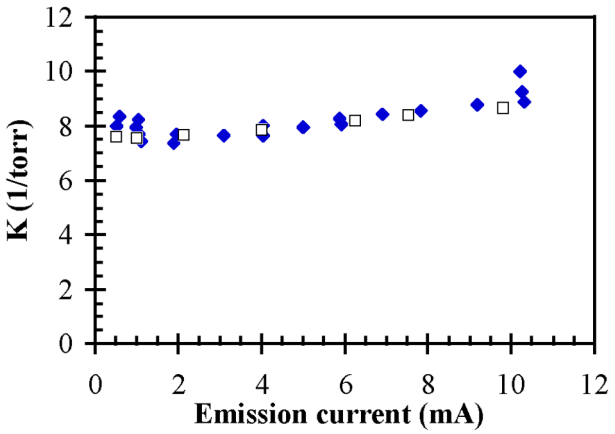

FIG. 8. (Color) The GESD Bayard-Alpert ion gauge is calibrated by comparison with a Granville Phillips Stabil-Ion gauge at two pressures: (blue diamonds) 6.5×10^{-7} torr and (open squares) 2.5×10^{-6} torr.

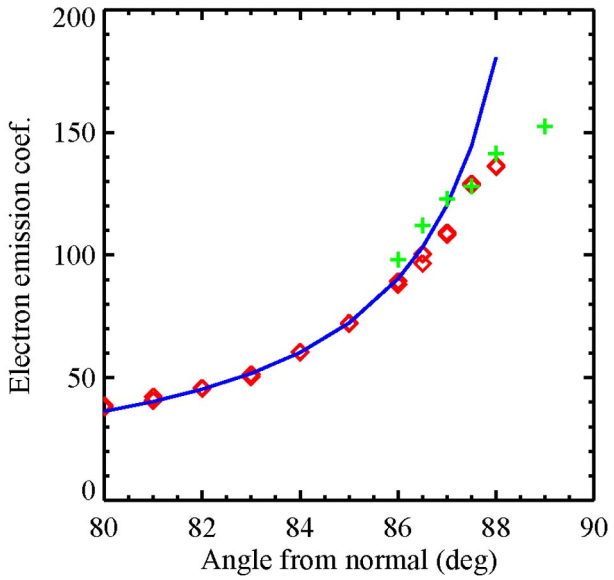

FIG. 9. (Color) Electron emission coefficient as a function of angle of incidence measured from normal for a baked target. Red diamonds indicate measurements (at least two data points per angle), the blue line is given by $6.3/\cos(\theta)$, the green (+) points are scaled with the SRIM code as in Eq. (8) [20].

dence of the electron emission coefficient on the angle of incidence [7],

$$\gamma_e \propto \frac{d}{\cos(\theta)}, \tag{5}$$

where $d/\cos(\theta)$ is the ion path length through a thin $d \approx 2$ nm thick surface layer (from which delta electrons can escape as secondaries). This can be combined with Rothard *et al.*'s expression for γ_e at normal incidence [29],

$$\gamma_e = 0.14 C_b \frac{dE}{dx}, \tag{6}$$

where $C_b \approx 0.32$ and dE/dx (eV/Å) is the electronic part of the energy loss per unit length [6,29]. Then the magnitude of γ_e at other angles is given by

$$\gamma_e = 0.045 \frac{dE}{dx} \frac{1}{\cos(\theta)}. \tag{7}$$

The electron emission falling below the $1/\cos(\theta)$ curve beyond 86° is attributed to large-angle nuclear scattering of ions out of the 2 nm layer [7]. We tested this model for our beam parameters with the SRIM 2003 code [20] by varying the thickness d of a thin foil with 1 MeV K^+ incident on 88°, until the transmitted distance (X from SRIM) normalized to $d/\cos(\theta)$ was near 0.75 [0.78 as shown in Fig. 9], the amount by which the measured γ_0 fell below $1/\cos(\theta)$. We then compute the secondary electron emission coefficient from

$$\gamma_e = \frac{X\cos(\theta)}{d} \frac{6.06}{\cos(\theta)} = \frac{6.06X}{d}. \tag{8}$$

We found that $d = 2.2$ nm satisfied this condition. Then using this thickness at other angles gave the green (+) points in Fig. 9, which are a reasonable fit to the data at angles near grazing incidence for which the $1/\cos(\theta)$ fit begins to fail. Published work at much lower energies showed the electron emission falling below the $1/\cos(\theta)$ curve beyond 20°–40° for 2–5 keV argon or neon ions onto a tantalum target [10]; these data are at least qualitatively consistent with nuclear scattering, which has a larger cross section at low ion energies. In fact, the data for the lowest energy ions falls below $1/\cos(\theta)$ at smaller angles from normal than for the higher energy ions in Ref. [10]. The authors do not draw this conclusion, but they separate the causes of emission into kinetic and potential energy, and conclude that the potential energy driven emission is independent of the ion angle of incidence.

Electron emission has also been measured at 20 °C–100 °C before baking, with sparser data than in Fig. 9, for which the target temperature was ~220 °C, after being baked *in situ* at that temperature for a total of 85 h. These are compared in Fig. 10. (Before baking, the target temperature ranged between room temperature and 100 °C due to heating by the ion gauge filament. The baking was performed in two sessions: During the first the target was at ~220 °C for 20 h, including a few hours during which the target reached 240°. During the second session the target temperature remained within 10 °C of 220 °C for 65 h. The box temperature reached 140 °C.) Two shots are shown at each angle before baking (black +), and after baking at least two shots are shown for each angle (three at 80° and 81°). No significant change is apparent in the electron emission after baking.

B. Space-charge limited emission current: possible errors and validity checks

We have noticed that it would be possible to obtain a secondary emission current that erroneously scales with $1/\cos(\theta)$ in two ways: (i) by operating in a space-charge current limited regime as we show below, and (ii) by beam-impact ionization of desorbed gas [30] that we will discuss in Sec. V B. The Child-Langmuir space-charge limit for electron current density is given by [26]

$$j = 2.3 \times 10^{-6} \frac{V^{3/2}}{d^2} \approx 2.4 \times 10^{-4}\ \mathrm{A/cm^2}, \tag{9}$$

where j is in $\mathrm{A/cm^2}$, the potential difference V (~ 190 V) between electrodes is in volts, and the gap between electrodes $d = 5$ cm. The target area is given by

$$A_T = 2.5\ \mathrm{cm} \frac{0.3\ \mathrm{cm}}{\cos(\theta)}, \tag{10}$$

where $4.3 \le A_T \le 21\ \mathrm{cm^2}$ at angles ranging from 80° to 88° for a beam defined by an aperture to be 2.5 cm wide

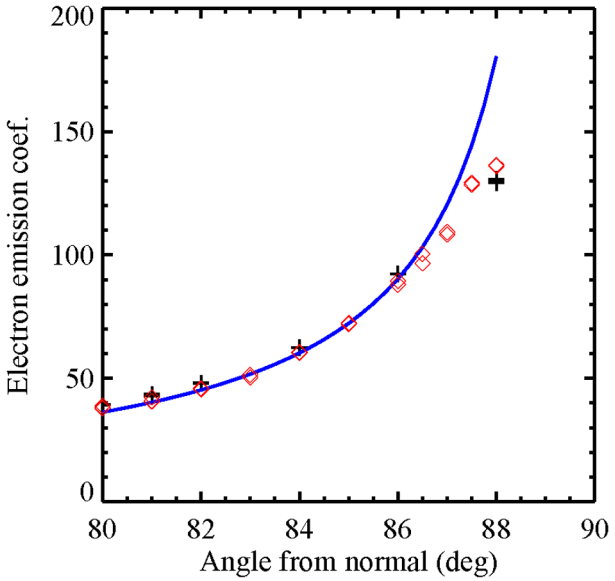

FIG. 10. (Color) Electron emission coefficient as a function of angle of incidence measured from normal, before (black +) and after baking at 220 °C for 85 h (red diamonds). The blue line is given by $6.3/\cos(\theta)$.

by 0.3 cm high. The total space-charge limited current then scales as

$$I \propto \frac{V^{3/2}}{d^2 \cos(\theta)}. \tag{11}$$

This would be misleading, giving an incorrect value for the secondary emission coefficient that is lower than the true value. We avoid this problem by reducing the beam current through varying the focusing strength of the final electrostatic quadrupole QI10, as was shown in Fig. 7.

Despite reducing the beam current we find that the measured emission current exceeds the calculated Child-Langmuir current limit of 0.8 mA at 78.25° by a factor of ≥ 5, Fig. 11. Although we have not determined the mechanisms by which the emission current apparently exceeds the Child-Langmuir current limit, we are convinced that the emission current is not space-charge limited for the data in this paper. This is because the time dependence of the $V_{\mathrm{QI10}} = 40$ kV emission currents shown in Fig. 11 is similar to that of the beam current measured by the GESD Faraday cup, consistent with not being space-charge limited: For these data, the current at $V_{\mathrm{QI10}} = 32$ and 36 kV exceeds that at our operating point of $V_{\mathrm{QI10}} = 40$ kV. The target emission current saturates for grid bias voltages exceeding +50 V [see Fig. 5(a)]. Finally, we have data that we will discuss next showing that the emission current, at all angles, is nearly independent of grid bias for bias voltages of +50, +100, or +150 V.

The data for Fig. 5 were taken at a single angle of incidence, 80°; perhaps other angles of incidence would show the current limited by space charge rather than emission? The following data demonstrates that is not the case. We measured the secondary emission as a function of angle, biasing the grid to +50, +100, and +150 V at each angle, as shown in Fig. 12. The order of points is 50 V at the bottom and 150 V at the top, except at 86.5° where 50 V is at the top; however, the data from different biases are closely spaced at every angle, and show a similar saturation of the current with bias voltage as shown in Fig. 5(a). The data are shown as emission current rather than electron emission coefficients because, at that time, we did not have a Faraday cup or other credible measurement of the beam current into the GESD. (Figure 12 would give similar emission coefficients to the data shown in Fig. 9 if the beam current into the GESD were about 0.2 mA compared with the present 0.14 mA.) These data demonstrate that the electron emission coefficients presented here are not in error from space-charge limits at any angle from 75° to 88°.

These data also demonstrate the reproducibility of electron emission measurements. The data were taken first at 88°, then stepping downwards from 86.5° to 75°. At the end, we returned to 87° (50 and 150 V grid bias) and 88° (100 V grid bias). Measurements taken at the end of the run are seen to agree well with those from the beginning.

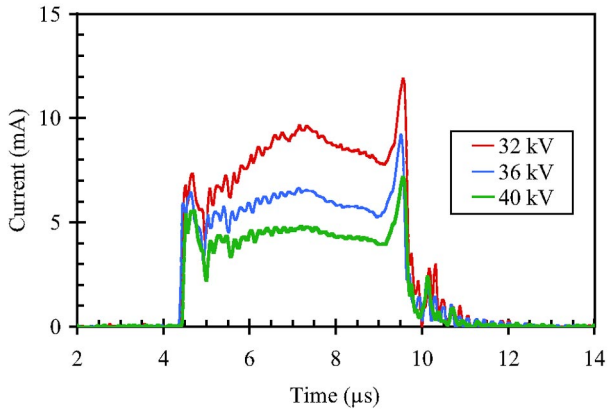

FIG. 11. (Color) Electron emission current from the GESD target versus time for three values of V_{QI10}, listed by the legend in the same order as the plots. (The normal operating point for other data in this paper is 40 kV.) The beam hits the target at $\theta = 78.25°$. The Child-Langmuir current limit is 0.8 mA. The spikes at the head and tail of the beam are a result of a mismatch of these parts of the beam, resulting in the head and tail having a smaller envelope than does the flattop of the beam, at the GESD axial position.

C. Electron energy distribution

The energy of emitted electrons can be obtained from the current-voltage characteristic where the grid voltage is varied, Fig. 5(a) [31]. The grid serves as a retarding potential analyzer for target emission because the grid is nearly parallel to the target. The grid is tilted by ~86° from normal to the beam, and the target is tilted 80° for these data, resulting in them being ~6° out of parallel.

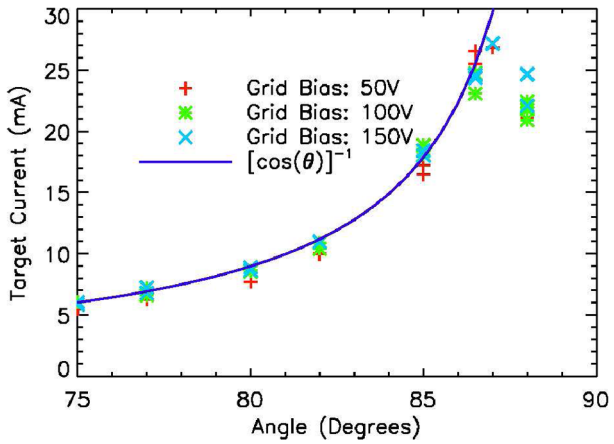

FIG. 12. (Color) Electron emission current as a function of angle of incidence measured from normal for grid bias of +50 V (red +), +100 V (green *), and +150 V (blue ×). The suppressor was biased to −50 V, the target to −40 V, and the catcher to −25 V.

Electrons with energy normal to the grid that is greater than the amount by which the grid bias is more negative than the target bias of −40 V can pass through the grid and contribute to the measured target current. Electrons of lower energy, normal to the grid, will be reflected back towards the target and will not contribute to the target current.

This measurement is approximate, because retarding potential analyzers measure only the component of energy normal to the electric field, but electrons are emitted over a broad angular distribution [32]. [True secondaries from electron impact have a $\cos(\theta)$ distribution [33].] Since the grid potential exists above, to both sides, and to the front of the target, the only other electrode that electrons can be deflected to is the catcher, back of the target. The current to the catcher is shown in Fig. 5(a) by the circular red points: as the grid bias becomes more negative, more electrons are deflected to the catcher resulting in its current becoming more negative; however, the change in catcher current is only 5% of the change in the target current so this correction is small and does not change the linear fit shown in Fig. 5(b). Returning an electron to the target, without it hitting another electrode, requires higher bias voltage on the grid than is required to prevent the electron from passing through the grid, therefore our measured temperature is expected to exceed the real electron temperature.

For ease in seeing whether the electron distribution approximates a Maxwellian, we plot the Fig. 5(a) data on a semilog scale after subtracting a new baseline drawn through the points at −300 and −200 V. The results, Fig. 5(b), show that the energy distribution is approximately Maxwellian over a factor of 40 in electron current; therefore, it is appropriate to refer to an electron temperature of 30 eV, rather than only an average energy. The points below 0.2 mA represent the most energetic electrons, which are less than 2.6% of the total emitted electrons, with an energy that is more uncertain than that of the bulk electrons emitted from the target under 1 MeV K^+ ion bombardment. Although we have evidence, which will be discussed in the next section, that the electrons measured here are born on (or in) the target, we observe in passing that electrons are Maxwellian when gas is ionized by ion impact. For example, 25 keV protons (same velocity as 1 MeV K^+) on H_2 and N_2 resulted in average electron energies of 12–14 eV that were Maxwellian over 4 orders of magnitude [34].

A survey of published measurements of secondary electron energy finds results obtained with a similar technique that agrees with ours; however, high resolution measurements of secondary electron energy distributions found energies of only a few eV for bombardment by MeV range protons or several keV range argon ions. These are discussed below. Secondary electron energies similar to our measurements were determined with a similar technique (i.e., similarly approximate) for 5–24 MeV protons bombarding aluminum-oxide and gold targets: half of the electrons had an energy below 20 eV [35]. Rothard *et al.*, measured the secondary electron energy spectrum with high resolution, from a carbon foil bombarded by 1.2 MeV protons [32]. The authors do not quote a temperature or average energy; however, the slope of their data corresponds to a bulk temperature of 3–4 eV, much lower than the results in Fig. 5(b) or Ref. [35]. The electron energy has also been measured with much higher resolution for various charge states of argon ions incident with energies of 3–6 keV on a tantalum surface [36]. Here the electron distribution peaks at 1–2 eV with few electrons above 10 eV. The consensus from these results would be that our electron energy measurement is about an order of magnitude high; however, it is also possible that 1 MeV K^+, which become ionized to charge states of 2.86 ± 1.55 in passing through a foil [37], which correspond to ionization potentials of 4.3–82.6 eV, do in fact generate higher energy electrons than do protons or low energy heavy ions.

V. GAS DESORPTION

A. Angular dependence

The gas desorption coefficient γ_0 is measured from the pressure rise after a beam pulse. This is shown in Fig. 13 for the target at 88°. We evaluate the pressure rise in two ways, as illustrated. The "peak" pressure rise is the maximum deviation of the averaged signal from the baseline, as shown by the horizontal blue line. We also fit an exponential decay to the data as shown by the straight red line on the semilog plot. (Both lines are drawn to illustrate our method, but may not agree precisely with the numeric fits that are used for the subsequent analysis.) If the desorption all occurs during the 5 μs FWHM of the beam, the extrapolated exponential decay should give the

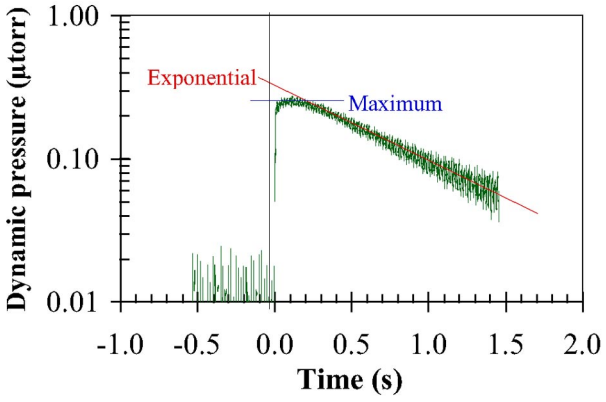

FIG. 13. (Color) The pressure rise measured by an ion gauge. The horizontal blue line indicates the peak excursion of the ion gauge current. The red line indicates a fit to the exponential decay of the ion gauge current, which we evaluate at $t = 0$.

most reliable value for γ_0. If the desorbed gas is released more slowly, γ_0 should be between the values plotted in Fig. 14.

The desorption coefficient is determined from the pressure rise ΔP(torr), the volume $V = 4180$ cm^3 of the GESD, the number of molecules per torr cm^3, and the number of beam ions into the GESD N_b to be

$$\gamma_0 \equiv \frac{3.3 \times 10^{16} V \Delta P}{N_b}. \tag{12}$$

Implicit in the use of Eq. (12) is the assumption that desorbed gas undergoes many bounces off interior surfaces in the GESD without either sticking to a surface or dislodging additional molecules, as was discussed in Sec. II B. The number of beam ions into the GESD is determined from integrating the current into the Faraday cup over the entire beam pulse duration

$$N_b = \int \frac{I_b}{1.6 \times 10^{-19}} dt. \tag{13}$$

The emission-from-a-thin-layer model used to explain the $1/\cos(\theta)$ dependence of electron emission would lead us to expect the same angular dependence if desorption is from adsorbed gas layers on the surface. The less than $1/\cos(\theta)$ dependence of gas desorption with angle, Fig. 14, indicates that it is not entirely from layers of gas adsorbed on the surface. (As with electron emission, we first show the larger data set, obtained after the target was baked for 85 h at ~220 °C.) This conclusion would be modified if the radial range of desorption around an ion track were comparable to or larger than the ion range. [Secondary emission is believed to occur within a small radius (few nm) of the ion track, which is much less than the 1 MeV K^+ range of ~500 nm and is therefore consistent with the observed $1/\cos(\theta)$ dependence on the ion angle of incidence.] We check this conjecture with a simple model, in which all atoms in a cylinder with length equal to the beam-ion range (~ 500 nm) share equally in the 1 MeV beam energy. The heat of vaporization for CO_2 is relatively high, H_2 is relatively low giving a range of 0.27 to 0.0093 eV/atom [25]. The heat of vaporization is similar to the energy required to remove an adsorbed molecule from multiple monolayers of gas. With these parameters, the radius of the heated cylinder will be in the range of 31–165 atoms. At 0.4 ± 0.1 nm average molecular diameter, the desorption diameter would fall between 25–132 nm. This is between 5% and 26% of the ion range, so we expect a $1/\cos(\theta)$ dependence for desorption of thin gas layers, with small departures from this scaling for low heat of vaporization gases like H_2 where the desorption diameter may reach 26% of the ion range. This conclusion would apply, even more strongly, to the much longer range 800 MeV lead ions studied by Mahner *et al.* [13] where the measured variation of desorption with angle also had much less than a $1/\cos(\theta)$ scaling.

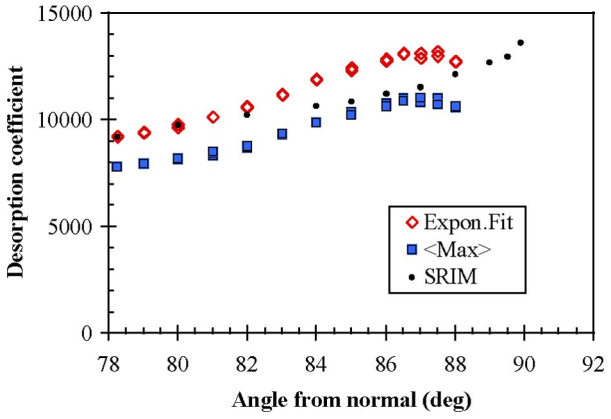

FIG. 14. (Color) Gas desorption coefficient as a function of angle of incidence measured from normal for a baked target. Open red diamonds represent the exponential fit to the ion gauge current evaluated at $t = 0$, the solid blue squares represent the peak pressure excursion measured by the ion gauge current. The filled black circles represent the effect of ion backscatter as predicted by the SRIM code, if desorption is independent of angle.

Approximate agreement with the measurements is obtained with a simple model that the desorption is independent of angle, but that ion backscattering provides an additional collision with the wall for ions near grazing incidence. Ion backscatter is predicted by the SRIM code, as in Fig. 3, but here it is calculated for 1.0 MeV K^+ ions. The result is shown in Fig. 14, normalized to the exponential fit data at 80°. The model fits well from 78°–82°, then falls below the data until near 88° where it crosses the data; overall, the variation with angle is not a good match to the data.

B. Mitigation techniques

We also measured the electron emission and gas desorption coefficients from a stainless steel surface that was roughened by blasting the surface with glass beads, Fig. 15. With the observed $6.3/\cos(\theta)$ electron emission coefficient, we expected bead blasting to reduce electron emission for ions near grazing incidence because these ions would then impact the rims of craters on the roughened surface at angles closer to normal. These data have larger variability because they were collected at the beginning of the commissioning phase of a beam line.

Future measurements with much higher reproducibility may enable us to infer real-time gas desorption coefficients during the beam duration. At least part of the beam passes through the desorbed gas layers since gas velocities are at least thermal (0.5 mm/μs), which would fill most of the 3 mm high beam in its 5 μs duration. Higher gas velocities, of ~2 mm/μs corresponding to 0.5 eV energies, are plausible for electronic desorption

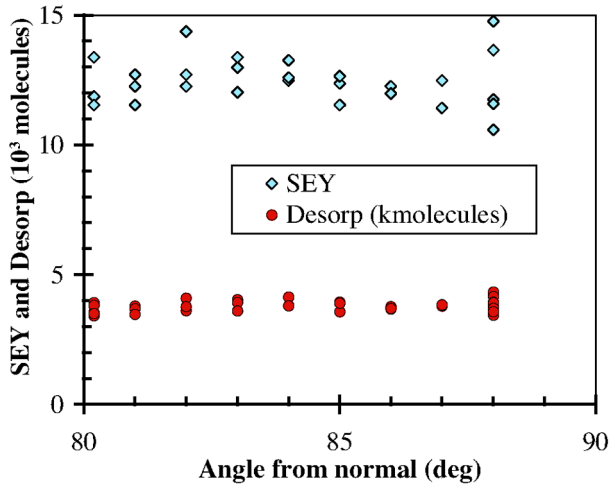

FIG. 15. (Color) The electron emission coefficient (SEY, blue diamonds) averages 12.5 ± 0.9 (standard deviation) and the gas desorption coefficient (red circles) averages $3.8(\pm 0.2) \times 10^3$ molecules for 1 MeV K^+ incident on stainless steel roughened by bead blasting.

processes (to be discussed in Sec. V D); this would fill the 3 mm high beam in 1.5 μs. The gas would be desorbed from the target area impinged by the beam, given by Eq. (10), that scales with $1/\cos(\theta)$. Ionization of this gas by beam impact would scale with the beam length in the gas, which is also proportional to $1/\cos(\theta)$, times the desorption coefficient [30]. Measuring a small component of $1/\cos(\theta)$ from a bead-blasted surface, and using estimated cross sections for beam ionization of gas, would then enable us to determine the gas desorption coefficient in the 5 μs while the beam is on. This would be an independent check on another method, which determined a desorption coefficient of ~900 from a perforated sheet of stainless steel by measuring the fraction of beam that was doubly ionized by passing through the desorbed gas [38]. The difference between that measurement and the measurements in this paper greatly exceeds the uncertainties expected from either method. One hypothesis to account for the difference is that much of the desorbed gas is delayed in its emission. Further discussion is beyond the scope of this paper and is left for a future publication.

Bead blasting produces small increases in surface area, as opposed to other traditional methods of reducing electron emission with a black labyrinth of deposited particles [33] where many emitted electrons are lost by hitting the surface before escaping; this increases the surface area by many times resulting in higher outgassing which is undesirable for ultrahigh vacuum. Similar results were reported for a small sample of copper, treated to produce a strongly dendritic surface that had secondary emission coefficients below 1 for electron impact, but which had a large surface area and was difficult to apply to a large scale accelerator [39].

Roughened beam-facing surfaces are a significant mitigation technique. (i) The electron emission in Fig. 15 decreased by up to a factor of 10 from that shown in Fig. 9. (ii) The gas desorption coefficient decreased by about a factor of 2 to 3. (iii) From the reduction in electron emission and the previously observed $1/\cos(\theta)$ dependence of electron emission, we can infer that the average angle of beam-ion incidence on the roughened surface was at 60° from normal. Then, from Fig. 3 we find that ions incident at 60° have a backscatter coefficient of 3% compared with higher than 60% for ions incident at 88°, a factor of more than 20 reduction in ion scattering.

Far higher reductions in ion scattering are predicted for scraping beam halos at normal incidence on apertures or sawtooth walls. Sawtooth walls are being developed at CERN for LHC and tested on SPS [23]; however, compared with roughened sheet metal, sawtooth surfaces are more difficult to fabricate as rectangular tubes and much more difficult to fabricate as circular or elliptical beam tubes, as LHC needs (and has developed). The alternative of beam-scraping apertures either reduces the clear bore significantly or requires a large number of apertures to eliminate grazing incidence collisions of halo ions with the beam tube. Bead blasting is an inexpensive method of reducing ion scattering and ion-induced electron emission and gas desorption, especially on complex shapes. The range of 1 MeV K^+ is less than 1 μm in stainless steel. All of the mitigation measures discussed in this paragraph will fail for longer range ions, which are so close to grazing incidence that they can drill through multiple "crater rims" on a roughened surface, or through multiple sawteeth or apertures, thereby emitting electrons and gas multiple times.

Care must be exercised with bead blasting to minimize warpage of the material. The 0.18 cm thick target used for Fig. 15 was treated with a standard-enclosed glass-bead blasting system and remained nearly flat. However a very light blasting of 0.04 cm stainless steel sheet, intended for beam tube use, warped it to an unusable degree. Better success resulted from blasting with fine aluminum-oxide powder at reduced pressure, where the warpage of 0.04 cm stainless steel was reduced to a very small, tolerable level, and the surface appeared to be very rough when viewed with magnification. We plan to test this surface treatment with a future GESD target to determine if it provides effective reduction in electron emission as observed in the data of Fig. 15.

A second mitigation technique that we tried is baking the target to ~220 °C (± 10 °C) for a total of 85 h. The results, before and after baking, are shown in Fig. 16, all data evaluated with the exponential fit to the pressure decay after a pulse, as was shown after baking in Fig. 14. The box, enclosing the GESD, reached 140 °C. (In unbaked operation, the target has been observed to reach 100 °C from heating by the ion gauge.) The baking

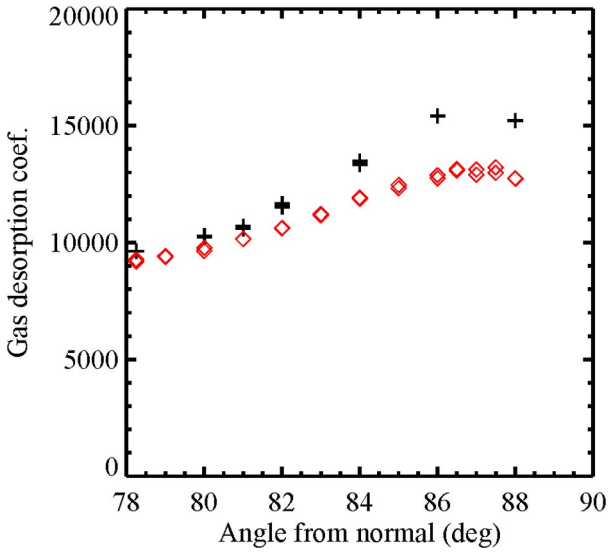

FIG. 16. (Color) Gas desorption coefficient as a function of angle of incidence measured from normal, before (black +) and after baking *in situ* (red diamonds) for 85 h at ~220 °C.

produced only a slight reduction in desorption, as shown by the results in Fig. 16, and no change in electron emission, as was shown in Fig. 10. The reproducibility was good: two shots are shown at each angle before baking (black +) except for 78.25° and 88°, and after baking at least two shots are shown for each angle (three at 80° and 81°). The effect of the baking was greatest at 86°–88° where the desorption was reduced by ~15% after baking. The baking would be expected to reduce one source, the amount of adsorbed gas on the surface, from which we expect a $1/\cos(\theta)$ scaling. Figure 16 is consistent with other sources of desorbed gas being both less affected by baking and more independent of angle. The implication is that much of the desorbed gas comes from sources that are unaffected by baking.

C. Surface impurity characterization

Gas desorption measurements at CERN used a calibrated residual gas analyzer to measure the partial pressures of selected mass gases [13]. They found that the dominant species were CO, CO_2, H_2, and CH_4, in that order. We measured the total pressure rise rather than each desorbed species. However, we have analyzed the surfaces of two samples (one stock, the other sanded, 0.18 cm thick stainless steel sheet) using both Auger electron energy spectroscopy (AES) and x-ray dispersion analysis (EDX), which analyzes the energy spectrum of x rays emitted by electrons from a scanning electron microscope striking the surface being analyzed. The results of the Auger spectroscopy are summarized in Table I, indicating that carbon and oxygen are the dominant impurities on or near the surface. The samples are exposed to monochromatic x rays at a 45° angle of incidence, for which atoms within 3 to 5 nm of the surface can be detected. (Note that since multiple electron shells are required to produce Auger electrons, hydrogen and helium cannot be detected directly and are not listed in the table.) EDX spectra were first taken with 15 keV electrons to verify that the underlying metal was stainless steel, then surface analysis data were taken with 6 keV electrons. Carbon, oxygen, and a small amount of silicon were the primary impurities found with EDX, in qualitative agreement with the Auger spectroscopy results. These results are compatible with having desorbed species similar to those measured at CERN.

An ion beam of 2 keV Ar^+ was used to remove surface layers by sputtering between Auger spectroscopy measurements. The sputtering was calibrated to sputter Ta_2O_5

TABLE I. Surface constituents in percent measured with Auger electron energy spectroscopy, from the electron shells listed in parenthesis for each element. The times listed are the cumulative sputtering duration.

Sample	t_{sput}(min)	C(1*s*)	O(1*s*)	Na(1*s*)	Si(2*p*)	Cr(2*p*)	Fe(2*p*)	Ni(2*p*)
Nominal 304 SS	···	≤ 0.08	···	···	≤ 1.00	18–20	68–74	8–12
Stock	0	15.36	61.49	0.69	8.20	4.09	3.65	0.06
	1	4.33	15.43	0.17	0.00	17.85	54.61	5.94
	2	5.40	6.98	0.00	0.00	16.58	68.94	0.57
	3	5.50	6.62	0.00	0.00	16.76	68.01	1.59
	4	5.84	6.91	0.11	0.00	17.28	67.84	0.83
	5	4.48	6.64	0.52	0.24	16.97	68.90	1.09
	15	3.74	6.82	0.00	0.00	18.19	69.81	1.00
Sanded	0	24.78	50.79	···	8.90	3.94	11.17	0.28
	1	5.14	21.47	···	1.06	12.16	57.51	2.65
	5	1.85	11.49	···	0.00	17.19	68.46	0.89
	15	3.68	5.82	···	0.00	12.49	77.34	0.62

at a rate of 4 nm/min; if the same order of magnitude sputtering is obtained with stainless steel, tens to hundreds of atomic layers are removed from each of the two samples in Table I. The times listed are cumulative sputtering durations.

In the "as received" condition, before sputter cleaning, we see in Table I that the metallic constituents of stainless steel (chromium, iron, and nickel) are almost absent from the near surface layers, instead the major constituents are carbon and oxygen. After 1–2 min of sputter cleaning, the chromium and iron approach their nominal values (listed in the top row in Table I), but the measured nickel content remains low. Most of the adsorbed gas is removed during the first minute of sputtering, giving little information on the depth of the adsorbed layers, other than it must have been at least 3 to 5 nm deep to obscure the substrate metal during the initial AES scan before sputtering. Some impurities such as sodium and silicon are only on the surface and disappear in 1–2 min of sputtering. (The silicon may be from silicon carbide which is used in certain varieties of Scotch-Brite, a mild abrasive pad, which was used to polish the target.) However, the major surface contaminants, carbon and oxygen, after decreasing by factors of 3 to 10 in the first 3 min of sputtering, then remain at a several percent level, even after 15 min of sputtering. This may be an artifact of the measurement, caused by knock-on collisions with argon ions driving impurities into the surface [40]; alternatively, the impurities may be present in some other form in addition to adsorbed gas layers (or several atomic-layer thick chromium-oxide for oxygen), as we also concluded from the dependence of the desorption coefficient on the ion angle of incidence, Fig. 14. Alternative forms of impurities, that might survive 15 min of sputtering or the baking of Fig. 10, include dust on the surface, inclusions and dissolved contaminants in the surface, and perhaps contaminants along grain boundaries.

D. Model for gas desorption

We compare two models for desorption: physical and electronic sputtering. "Sputtering" is usually used to mean physical sputtering. Physical sputtering results from the nuclear scattering component of dE/dx that can scatter ions through a large angle with a correspondingly large momentum imparted to the sputtered atom. Electronic sputtering is due to the electronic component of dE/dx [41,42]. The values of dE/dx can be evaluated with the SRIM code [20] and are shown for K^+ ions incident on stainless steel in Fig. 17. The electronic component exceeds the nuclear component for K^+ ions with energy exceeding 250 keV. We see that for K^+ at 1 MeV the electronic component has 4.6 times as much energy available near the surface as does the nuclear component. It is therefore plausible that electronic energy loss provides the energy source for the large gas

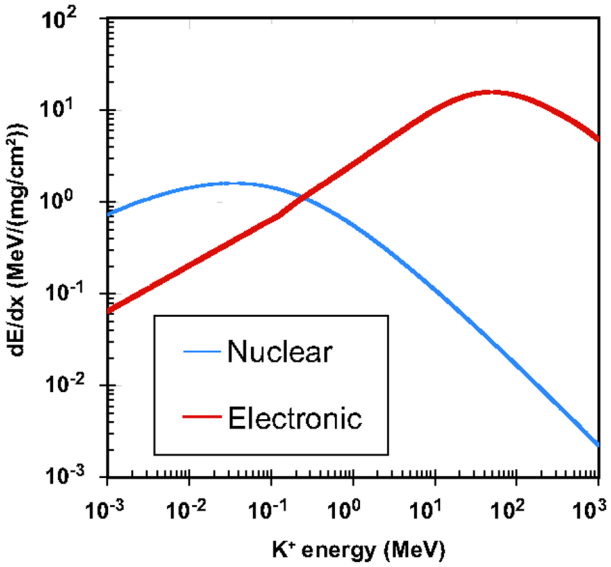

FIG. 17. (Color) The ion energy loss due to nuclear large-angle scattering (blue line) and to interaction with electrons (thick red line) is shown versus energy for K^+ ions incident on stainless steel.

desorption coefficients that we measure. This model is related to the accepted model for electron emission due to ion impact: the delta electrons that are pulled out of atoms in the material may escape the surface if released sufficiently close to the surface—usually taken to be within 1 to 3 nm of the surface [7].

The concept of electronic sputtering is relatively new [41,43]. The initial experiments were to study the effects of Voyager spacecraft observations: that icy objects in the outer solar system were exposed to energetic plasma-ion bombardment [44]. Application to accelerators has been limited to gas desorption from cryopanels bombarded by stray particles [45]. Molecular dynamics (MD) modeling of ions impinging on insulators has been used with considerable success to explain the sputtering of frozen ices, especially of H_2O and noble gases [44]. It has been applied to explain the atmospheres of moons of Jupiter and Saturn and the rings of Saturn as a result of ion bombardment of frozen ice on the surfaces [42].

The major difficulty with the MD modeling of electronic sputtering for desorption from accelerator beam tubes is that it is not expected to be applicable to ions impinging on metals for two major reasons.

(i) The electronic contribution to thermal conductivity that is dominant in metals is not present in a classical MD simulation. As a result the total thermal conductivity is significantly underestimated. This leads to unphysical confinement of the deposited energy in the surface region of the irradiated target or within the region excited by an energetic ion and does not allow for the direct comparison between the calculated and experimental data.

(ii) MD does not provide a mechanism for energy exchange between the electrons and the lattice. Some

current codes use a friction force to account for electronic stopping power, but still do not allow for energy transfer from the electrons to the lattice [46,47].

A partial resolution of the difficulty comes from the measurements at CERN that found the dominant desorbed gases to be CO, CO_2, H_2, and CH_4, in that order [13]. All of these will be insulators when in solid or liquid form, with which the ion beam could interact in a classic MD simulation and cause electronic sputtering. However, classical MD simulation would not address the issue of whether beam interactions with the metal substrate could desorb volatile impurities that were in contact with the metal. We note that the physics of electrons interacting with potentially volatile molecules near a surface in electronic sputtering is closely related to the physics of desorption by electrons or photons incident on a surface.

The compelling motivation to use this model is that much more energy is available from electronic stopping than from nuclear stopping in the energy range for heavy-ion fusion, and even more so for high-energy physics. With physical sputtering from the nuclear scattering, it is difficult to get coefficients greater than a few tens, but electronic sputtering is energetically capable of producing desorption coefficients in the range of thousands as observed here and at other laboratories [1,13,14].

ACKNOWLEDGMENTS

Excellent technical support was provided by Ron Beggs (who constructed the GESD), Tak Katayanagi (who currently maintains it), Craig Rogers (who constructed and maintained the electronics), and their supervisors Ralph Hipple and William Strelo. We acknowledge the support and encouragement of Grant Logan. We have had productive discussions with Andris Faltens, Miguel Furman, Andreas Krämer, Edgar Mahner, Hartmut Reich-Sprenger, Wolfgang Stoeffl, and Peter Stoltz. Akiro Sakumi worked with us for two weeks during a U.S./Japan exchange. Thomas Schenkel suggested the possibility of electronic sputtering accounting for the large desorption coefficients observed and Eduardo Bringa has educated us further. We thank Cheryl Evans for surface analyses with Auger spectroscopy and James Ferreira for surface analyses with a scanning electron microscope and with EDX data. This work was performed by the University of California Lawrence Livermore National Laboratory under the auspices of the U.S. Department of Energy under Contract No. W-7405-ENG-48 and Lawrence Berkeley National Laboratory Contract No. DE-AC03-76F00098.

[1] S. Y. Zhang, in *Proceedings of the ICFA Workshop on Beam Induced Pressure Rise in Rings, Brookhaven National Laboratory, Upton, NY, 2003*, http://www.cad.bnl.gov/icfa.

[2] *Proceedings of the CERN eCloud'02 Workshop, Geneva, 2002*, http://wwwslap.cern.ch/ collective/ecloud02/proceedings/index.html.

[3] R. O. Bangerter, Philos. Trans. R. Soc. London A **357**, 575 (1999).

[4] A. W. Molvik *et al.*, in *Proceedings of the IEEE Particle Accelerator Conference, Portland, OR, 2003* (IEEE, Piscataway, NJ, 2003), p. 312.

[5] R. H. Cohen, A. Friedman, S. M. Lund, A. W. Molvik, M. Furman, J.-L. Vay, and P. Stoltz, in *Proceedings of IEEE Particle Accelerator Conference, Portland OR, 2003* (Ref. [4]), p. 132.

[6] P. H. Stoltz, M. A. Furman, J.-L. Vay, A. W. Molvik, and R. H. Cohen, Phys. Rev. ST Accel. Beams **6**, 054701 (2003).

[7] P. Thieberger, A. L. Hanson, D. B. Steski, S. Y. Z. V. Zajic, and H. Ludewig, Phys. Rev. A **61**, 042901 (2000).

[8] A. Clouvas, C. Potiriadis, H. Rothard, D. Hofmann, R. Wünsch, K. O. Groeneveld, A. Katsanos, and A. C. Xenoulis, Phys. Rev. B **55**, 12 086 (1997).

[9] A. Itoh, T. Majima, F. Obata, Y. Hamamoto, and A. Yogo, Nucl. Instrum. Methods Phys. Res., Sect. B **193**, 626 (2002).

[10] T. Kanie, A. Ichimiya, S. Ohtani, H. Tawara, and T. Yasue, Nucl. Instrum. Methods Phys. Res., Sect. B **67**, 601 (1992).

[11] J. W. McDonald, D. Schneider, M. W. Clark, and D. Dewitt, Phys. Rev. Lett. **68**, 2297 (1992).

[12] F. Aumayr, H. Kurz, D. Schneider, M. A. Briere, J. W. McDonald, C. E. Cunningham, and H. Winter, Phys. Rev. Lett. **71**, 1943 (1993).

[13] E. Mahner, J. Hansen, J.-M. Laurent, and N. Madsen, Phys. Rev. ST Accel. Beams **6**, 013201 (2003).

[14] E. Mustafin, O. Boine-Frankenheim, I. Hofmann, H. Reich-Sprenger, and P. Spiller, Nucl. Instrum. Methods Phys. Res., Sect. A **510**, 199 (2003).

[15] R. Behrisch, V. M. Prozesky, H. Huber, and W. Assmann, Nucl. Instrum. Methods Phys. Res., Sect. B **118**, 262 (1996).

[16] H. F. Winters and P. Sigmund, J. Appl. Phys. **45**, 4760 (1974).

[17] R. Bastasz and L. G. Haggmark, J. Nucl. Mater. **103**, 499 (1981).

[18] P. A. Seidl *et al.*, in *Proceedings of the IEEE Particle Accelerator Conference, Portland, OR, 2003* (Ref. [4]), p. 536.

[19] L. R. Prost *et al.* (to be published).

[20] J. F. Ziegler, http://www.srim.org/.

[21] J. F. Ziegler, J. P. Biersack, and U. Littmark, *The Stopping and Range of Ions in Solids* (Pergamon, New York, 1985).

[22] A. Faltens (private communication).

[23] V. Baglin, I. R. Collins, O. Gröbner, C. Grünhagel, and B. Jenninger, in *Proceedings of the European Particle Accelerator Conference, Paris, 2002* (EPS-IGA and CERN, Geneva, 2002), p. 2535.

[24] K. Kennedy, LBNL Report No. LSME-323, 1990.

[25] P. A. Redhead, J. P. Hobson, and E. V. Kornelsen, *The Physical Basis of Ultrahigh Vacuum* (Chapman and Hall, London, 1968).

[26] I. Langmuir and K. T. Compton, Rev. Mod. Phys. **3**, 244 (1931).

[27] A.W. Molvik, A. Friedman, G.W. Kamin, T.C. Sangster, S. Eylon, and H.S. Hopkins, Bull. Am. Phys. Soc. **42**, 2026 (1997).
[28] M. A. Furman and M.T.F. Pivi, Phys. Rev. ST Accel. Beams **5**, 124404 (2002).
[29] H. Rothard, K. Kroneberger, A. Clouvas, E. Veje, P. Lornezen, N. Keller, J. Kemmler, W. Meckbach, and K.-O. Groeneveld, Phys. Rev. A **41**, 2521 (1990).
[30] W. Stoeffl (private communication).
[31] A.W. Molvik, Rev. Sci. Instrum. **52**, 704 (1981).
[32] H. Rothard *et al.*, Nucl. Instrum. Methods Phys. Res., Sect. B **48**, 616 (1990).
[33] H. Bruining, *Physics and Applications of Secondary Electron Emission* (Pergamon, London, 1954).
[34] M. E. Rudd, Phys. Rev. A **20**, 787 (1979).
[35] J. E. Borovsky, D. J. McComas, and B. L. Barraclough, Nucl. Instrum. Methods Phys. Res., Sect. B **30**, 191 (1988).
[36] T. Kanie, K. Oda, A. Ichimiya, and T. Yasue, Surf. Sci. **242**, 417 (1991).
[37] K. Shima, N. Kuno, M. Yamanoichi, and H. Tawara, At. Data Nucl. Data Tables **51**, 173 (1992).
[38] F. Bieniosek (private communication).
[39] V. Baglin, J. Bojko, O. Gröbner, B. Henrist, N. Hilleret, C. Scheuerlein, and M. Taborelli, in *Proceedings of the European Particle Accelerator Conference, Vienna, 2000*, http://accelconf.web.cern.ch/accelconf/, p. 217.
[40] A. J. Nelson (private communication).
[41] W. L. Brown, W. M. Augustyniak, L. J. Lanzerotti, R. E. Johnson, and R. Evatt, Phys. Rev. Lett. **45**, 1632 (1980).
[42] R. E. Johnson, Rev. Mod. Phys. **68**, 305 (1996).
[43] W. L. Brown, L. J. Lanzerotti, J. M. Poate, and W. M. Augustyniak, Phys. Rev. Lett. **40**, 1027 (1978).
[44] R. E. Johnson, *Energetic Charged Particle Interactions with Atmospheres and Surfaces* (Springer-Verlag, Berlin, 1990).
[45] C. Benvenuti, R. Calder, and O. Gröbner, Vacuum **37**, 699 (1987); **38**, 145 (1988).
[46] E. Bringa (private communication).
[47] A. Caro and M. Victoria, Phys. Rev. A **40**, 2287 (2002).